

## A COMPARATIVE AND EXPERIMENTAL STUDY ON THE EFFECT OF HEAT TREATMENT CYCLES FOR PBF Ti6Al4V

M. Karasoglu\*, E. Yasa<sup>†</sup>, E. Tan<sup>\*\*</sup>, A. Yağmur<sup>‡</sup>

\*Eskisehir Technical University, Eskisehir, Turkey

<sup>†</sup>Eskisehir Osmangazi University, Eskisehir, Turkey

\*\* ASELSAN Inc, Ankara, Turkey

<sup>‡</sup> EOS GmbH, Krailling, Germany

### **Abstract**

Powder bed fusion (PBF) presents the highest level of technological maturity and industrialization level for metallic materials among other Additive Manufacturing technologies. The advantages of high geometrical complexity, ability to produce internal cavities, reduced lead time and buy-to-fly ratio enables a wide range of application areas from aerospace to biomedical. Laser-PBF and Electron-PBF present different limitations and opportunities while they can both build from Ti6Al4V powder. The performance of the E-PBF and L-PBF parts highly depends on the resulting microstructures and differs significantly due to various mechanisms such as preheating temperatures and processing environment. Moreover, the obtained material properties generally necessitate heat treatments for reducing residual stresses, enhancing mechanical properties and changing the microstructure. This study aims to investigate the effect of the same heat treatment cycles on the E-PBF and L-PBF microstructure evolution and microhardness by a comparative experimental work with several combinations of exposure durations, temperatures and cooling rates.

**Keywords:** Laser Powder Bed Fusion (L-PBF), Electron Powder Bed Fusion (E-PBF), Heat Treatment, Microstructure

### **Introduction**

Additive Manufacturing (AM), also known as 3D Printing, is a new group of technologies based on layerwise production enabling very complex part geometries in contrast to subtractive manufacturing processes. Powder bed fusion (PBF), is one of the 7 sub-groups of AM technologies according to ASTM classification[1]. PBF methods, excluding Selective Heat Sintering, employ a laser or an electron beam to provide a high energy to melt or to sinter powder particles. All PBF processes include spreading of powder material over a base plate or previously solidified layers although different mechanisms may be employed in various processes. The most commonly used PBF processes for metallic parts are Laser-Powder Bed Fusion (L-PBF), also known as Selective Laser Melting or Direct Metal Laser Sintering/Melting and Electron-Powder Bed Fusion (E-PBF), also known as Electron Beam Melting. Although there are some similarities between L-PBF and E-PBF processes, they have some major differences leading to significant changes in the obtained part properties. In the E-PBF process, due to the presence of an electron beam, the process is carried out under vacuum and high preheating temperatures are applied in order to provide necking in between loose powder particles to avoid smoke formation during scanning. In the L-PBF process, whereas, the preheating temperatures are quite limited up to 200 °C in most applications

and the process is carried out under a protective atmosphere supplied by argon or nitrogen flow. The main differences between two processes are summarized in Table 1.

PBF of materials lead to many advantages compared to conventional manufacturing. First of all, the waste material related to subtractive machining in the form of machining chips is very much reduced since the manufacturing route is additive. This significantly reduces the buy-to-fly ratio in aerospace applications dealing with expensive materials. Moreover, very complex geometries including internal channels, cavities or lattice structures are possible with a relatively good dimensional accuracy. Moreover, using PBF, it is possible to produce mono-parts rather than assemblies reducing the need for joining processes and lead time. This may also lead to increase in the life-time of the parts since joining processes such as welding are generally limiting factors in terms of life assessment.

**Table 1:** Comparison of E-PBF and L-PBF processes

Property	E-PBF	L-PBF
<b>Energy Source</b>	Electron	Laser
<b>Beam Size [2]</b>	0.2-1 mm	0.1-0.5 mm
<b>Maximum Build Volume [3]</b>	350 x 380 mm (Ø/H) (Arcam Q20plus)	800 x 400 x 500 mm (Concept Laser X Line 2000R)
<b>Layer Thickness</b>	50-100 µm	20-100 µm
<b>Minimum Wall Thickness [4]</b>	0.6 mm	0.2 mm
<b>Build rate [cm<sup>3</sup>/h] [5]</b>	80	5-20
<b>Dimensional Accuracy [4]</b>	±0.3 mm	±0.1 mm
<b>Surface Roughness (R<sub>a</sub>) [5]</b>	20-30 µm	5-15 µm
<b>Geometry Limitations</b>	Powder sintering due to high preheating temperatures in internal features	Support structures are needed for overhang surfaces with low angles
<b>Available Materials</b>	Only conductive materials: Ti alloys, Titanium Aluminides, CoCr alloys, Inconel 718	Stainless steels, tool steels, maraging steel, nickel superalloys, Ti and its alloys, CoCr alloys, precious metals, Al alloys, Cu alloys

As shown in Table 1, titanium alloys can be processed by both PBF methods. Ti6Al4V alloy is the mostly addressed Ti-alloy in AM due to its superior biocompatibility, excellent corrosion resistance, high specific strength, high melting temperature and high fracture toughness [6]. It is an  $\alpha + \beta$  titanium alloy saving weight for highly loaded structural parts, especially in aerospace applications. Although this alloy is widely utilized in a wide range applications from marine, biomedical to chemical industries, some properties of Ti6Al4V alloys make it difficult to process including low thermal conductivity, high reactivity and its sensitivity to strain hardening [7-10]. Thus, it is difficult and costly to machine this alloy making AM a good choice [11-13].

In PBF processes, generally different microstructures are obtained due to high cooling rates leading to different mechanical properties in comparison to cast and wrought materials and Ti6Al4V is no exception. Figure 1 shows the phase diagram and phase transformation as a function

of cooling rate for Ti6Al4V. As shown, the formation of  $\alpha'$  martensite necessitates a specific thermal history with high cooling rates along with build temperatures lower than the martensite start temperature ( $M_s$ ). This martensite start temperature depends on the initial microstructure, composition homogeneity and impurity levels ranging from 575°C to 800 °C. A complete  $\alpha'$  martensite can form for cooling rates greater than 410 °C/s whereas low cooling rates smaller than 20 °C/s will not form  $\alpha'$  martensite.

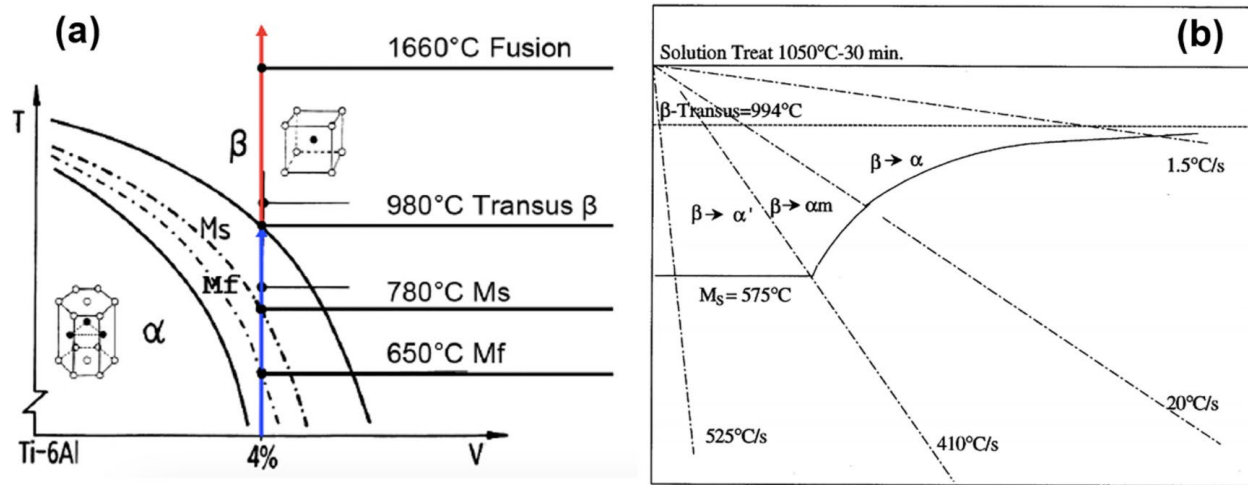


Figure 1: (a) Phase diagram of Ti6Al4V (b) Phase transformation as a function of cooling rates [6]

In the literature, L-PBF and E-PBF processes have been shown to form different microstructures. L-PBF is related to fine needle-shaped  $\alpha'$  martensite, with a typical lath width about 0.2–1  $\mu\text{m}$  whereas for E-PBF leads to  $\alpha + \beta$  dual phase, where the  $\alpha$ -lath has an average length and thickness of 1–3  $\mu\text{m}$  and 0.5–1  $\mu\text{m}$ , respectively while  $\beta$  platelets are about 0.1  $\mu\text{m}$  thick [6]. This difference in the microstructures between L-PBF and E-PBF processes is attributed to the thermal histories due to different preheating temperatures. The high preheating temperature in E-PBF acts as an in-situ heat treatment of  $\alpha'$  martensite and decomposition into  $\alpha + \beta$  microstructure [14–17]. With a similar approach, it is also possible to produce  $\alpha + \beta$  microstructure in as-built L-PBF parts as well by using a low laser power and a low scan speed to enable a long material-laser interaction time and high energy input [18].

After PBF of Ti6Al4V, heat treatments are applied for reducing residual stresses, enhancing mechanical properties and varying the microstructure of the produced parts. Various researchers have focused on the effect of heat treatments on different aspects such as mechanical properties [19, 20], fatigue performance [21–24], dimensional accuracy, corrosion resistance[25], biocompatibility [26], creep behavior [27], etc. In comparison to L-PBF, the number of studies on the heat treatment of E-PBF is much lower[11]. Moreover, there are very few number of studies investigating the effect of different heat cycles on the obtained microstructures from L-PBF and E-PBF processes. Therefore, this study aims to reveal and understand the effect of soak duration,

temperature and cooling rate in a heat treatment cycle on the microstructure of as-built E-PBF and L-PBF in a comparative way.

### **Experimental Methodology**

In order to understand the effect of different heat treatment cycles on the PBF parts, the specimens were first produced. The L-PBF specimens were produced on an EOS M290 machine under argon environment with a layer thickness of 40  $\mu\text{m}$  whereas the E-PBF parts were produced on an ARCAM A2X machine in vacuum with a layer thickness of 50  $\mu\text{m}$ . The process parameters for both machines are the standard ones which were optimized for maximum density.

After the productions were complete, the parts were cut off from the base plates and heat treated in Protherm PLF 130/6 furnace under ambient atmosphere in order to understand the oxide layer formation on the surfaces and microstructure evolution in the core of the part. The test plan with different heat cycles is presented in Table 2.

**Table 2:** Test Plan

	Temperature ( $^{\circ}\text{C}$ )	Duration (h)	Cooling Rate
1	1020	1	Furnace Cool
2	1020	2	Furnace Cool
3	940	2	Air Cool
4	940	2	Furnace Cool
5	900	2	Furnace Cool
6	850	2	Furnace Cool
7	850	5	Furnace Cool
8	850	8	Furnace Cool
9	800	2	Air Cool
10	800	2	Furnace Cool
11	800	4	Air Cool
12	800	4	Furnace Cool
13	730	2	Furnace Cool

After the heat treatments were applied, the specimens were cut showing the planes parallel to the build direction and mounted in a resin and polished to a mirror finish. In order to reveal the microstructures, a solution of 91 ml water, 6 ml  $\text{HNO}_3$  and 3 ml HF (Kroll's reagent) was used as the etchant and applied to surfaces. For quantitative analysis of microstructural images, image analysis was carried out by using FIJI software package. Different phases ( $\alpha$  and  $\beta$ ) in the OM images were classified by Trainable Weka Segmentation Fiji plugin. For classifications, a random forest classifier with 2 random features, 200 decision trees, 2 decimal places for computational accuracy, and 5 image filters (Gaussian blur, Hessian matrix, Sobel, Gaussian distribution difference, and membrane projection) was utilized. Subsequent to image classifications, segmentation processes were applied to  $\alpha$  phases in the images in order to evaluate individual  $\alpha$  particles. Segmentations were performed with "Disconnect particles" Xlib plugin for FIJI using a modified watershed algorithm. In this method, particles are disconnected according to predefined

constraint proportionality constant ( $k=0.7$ ) [28]. Image analysis was limited to the heat treated samples at 850°C or higher temperatures due to the resolution limitation of OM.

## **Results and Discussion**

### ***As-built microstructures***

First of all, as-built microstructures coming from L-PBF and E-PBF processes have been investigated. The microstructures are presented in Figure 2. As evident, while L-PBF sample exhibits a martensitic microstructure  $\alpha'$  acicular grains, E-PBF sample reveals lamellar  $\alpha+\beta$  basketwave (Widmanstätten) structure. Both microstructures are identical to manufacturing method. It is well known that difference between those two microstructures is due to higher solidification rate and lower process chamber temperature of L-PBF in comparison to E-PBF [29].

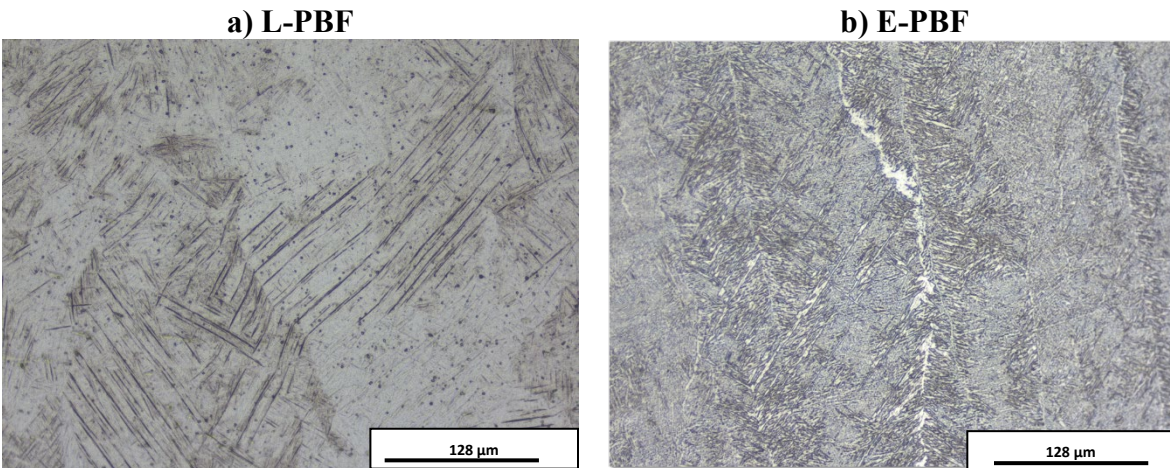


Figure 2: As-built microstructures from a) L-PBF b) E-PBF

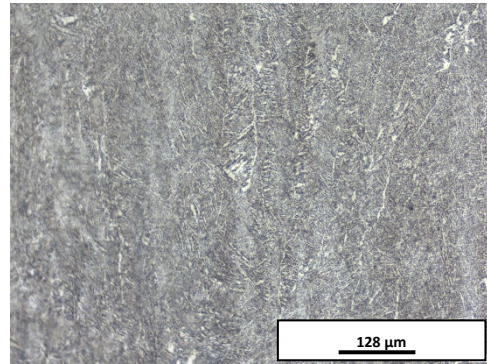
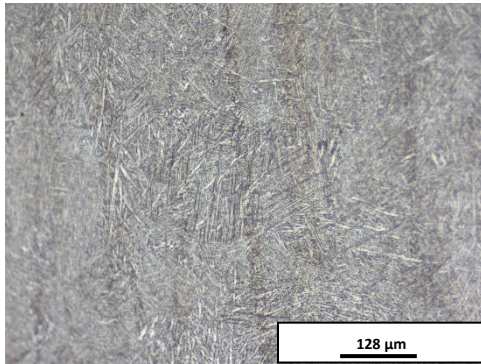
### ***Effect of annealing temperature***

The annealing temperature was varied between 730 and 1200 °C in this study in order to understand the evolution of the microstructure from L-PBF and E-PBF processes in a wide range of temperatures as demonstrated in Figure 3. While the temperature was changed, the time and cooling rate were fixed. All images in Figure 3 are belong to furnace cooled samples and annealing temperature was fixed to 2h.

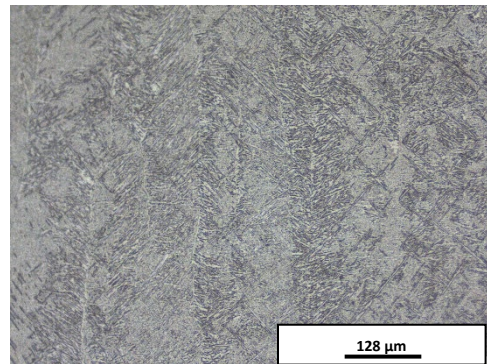
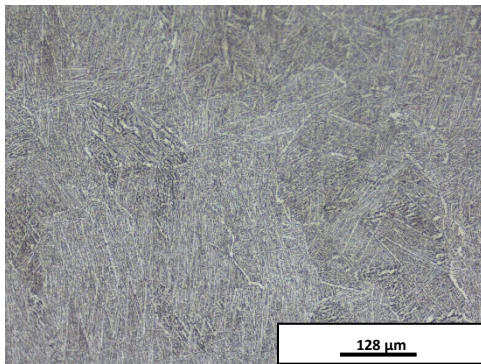
**L-PBF**

**E-PBF**

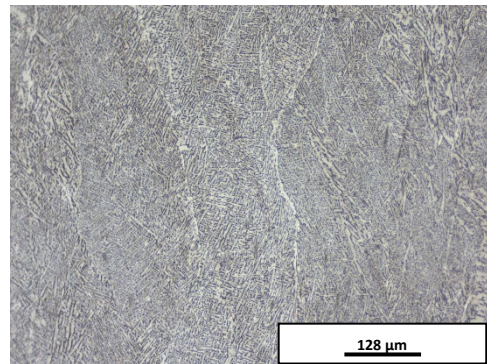
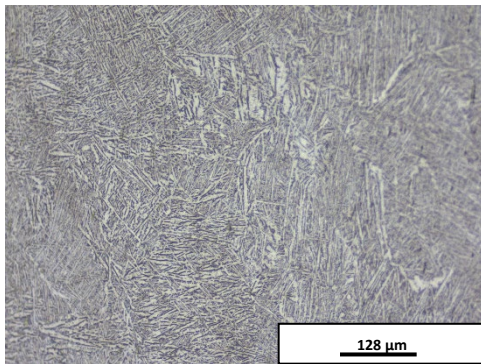
@730 °C 2h



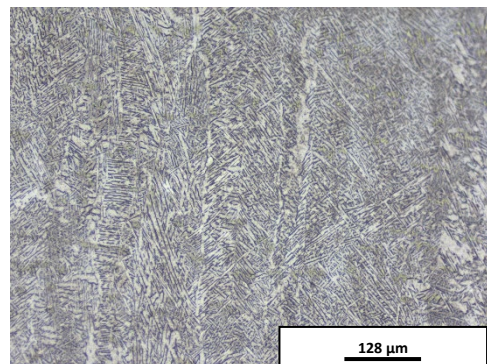
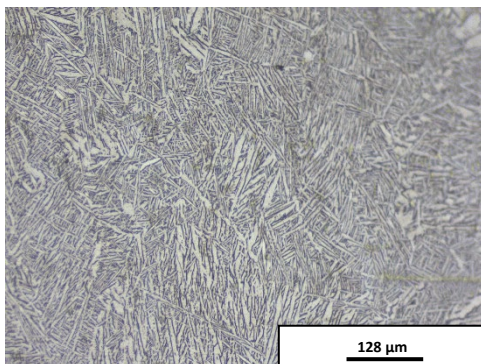
@800 °C 2h



@850 °C 2h



@900 °C 2h



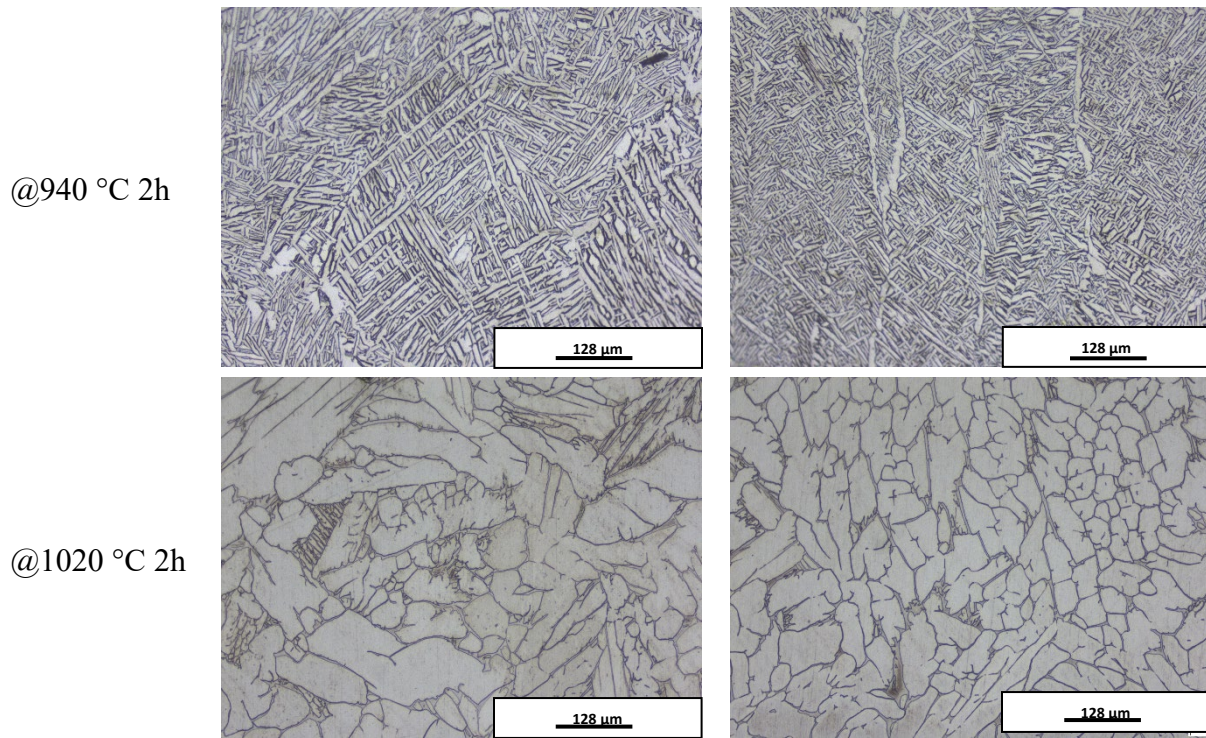


Figure 3: Effect of the annealing temperature

The results show that annealing temperature is a very important parameter to alter the microstructures for both L-PBF and E-PBF samples. It can be seen from the Figure 3 that lower temperatures ( $<900^{\circ}\text{C}$ ) have minor effect on microstructures and almost no visible difference from the as-built samples was observed with OM. Moderate annealing temperatures ( $900^{\circ}\text{C}$  and  $940^{\circ}\text{C}$ ) which are below the beta transus temperature modified microstructures to some extent. It can be seen that  $\alpha$  lath thicknesses of E-PBF samples were increased by heat treatments with moderate temperatures and fully  $\alpha'$  structure of the L-PBF samples were converted to  $\alpha+\beta$  two-phase microstructure. However, columnar parent  $\beta$  structures were not modified. On the other hand, high temperature (above transus temperature) annealing induced major changes in the microstructures of both E-PBF and L-PBF samples. High temperature annealing transformed parent  $\beta$  columns to uniform equiaxed grains and needle-like  $\alpha$  laths to globular  $\alpha$  grains.

#### ***Effect of annealing duration***

In order to test of the annealing duration, heat treatments were applied at  $850^{\circ}\text{C}$  for 2, 5 and 8 hours with furnace cooling. Moreover, tests were carried out at  $1020^{\circ}\text{C}$  for 1 and 2 hours. The results are depicted in Figure 4 and Figure 5.

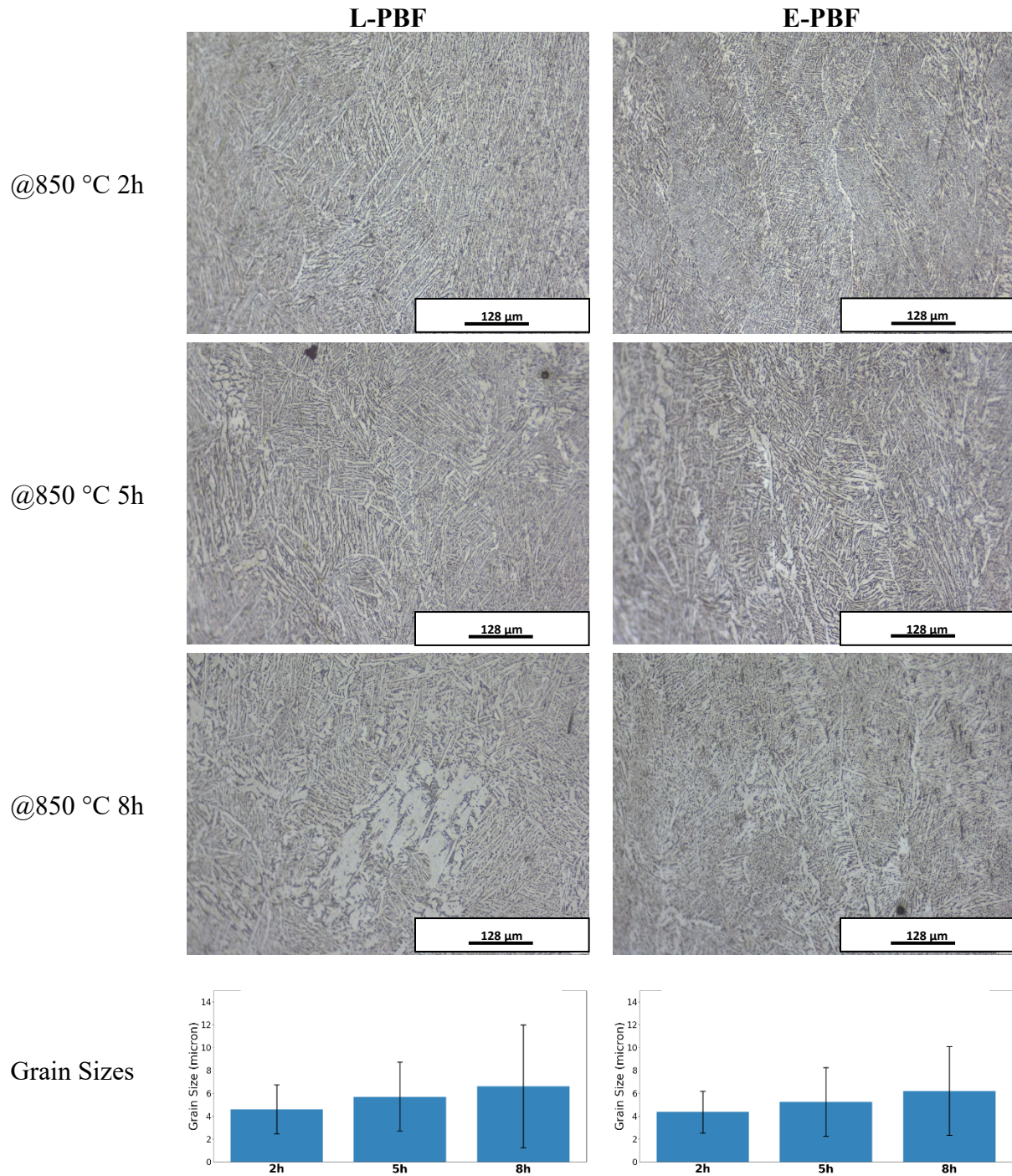


Figure 4: Effect of the duration at maximum temperature of 850 °C for furnace cooling

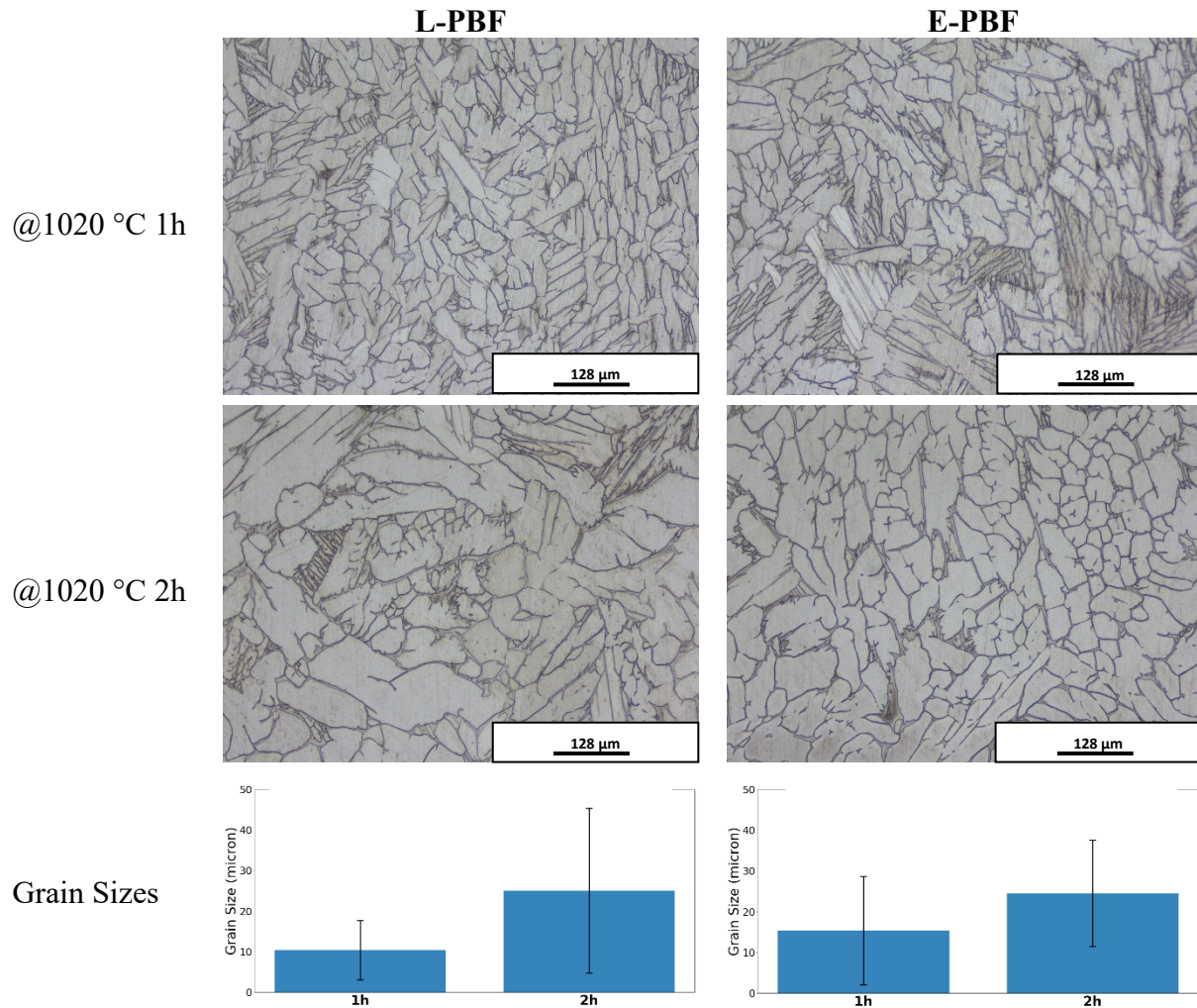


Figure 5: Effect of the duration at maximum temperature of 1020 °C for furnace cooling

The obtained results lead to the fact that increasing annealing duration increases size of  $\alpha$  grains. For the samples annealed at 850°C, increasing annealing time from 2h to 5h slightly increased grain sizes and grain morphology was maintained. However, the samples annealed for 8h displayed locally globular grains in the microstructure. In high temperature heat treatments, the effect of the heat treatment time is more evident on the grain size and shape of the  $\alpha$  grains. Figure 5 shows that increasing annealing time from 1 to 2h, grain size of the samples were nearly doubled and almost all  $\alpha$  grains were transformed to a globular shape.

#### ***Effect of cooling rate***

As shown in Table 2, the effect of cooling rate was tested at 940°C and at 800°C for 2 and 4 hours. The obtained microstructures for L-PBF and E-PBF processes are presented in Figure 6 and Figure 7, respectively.

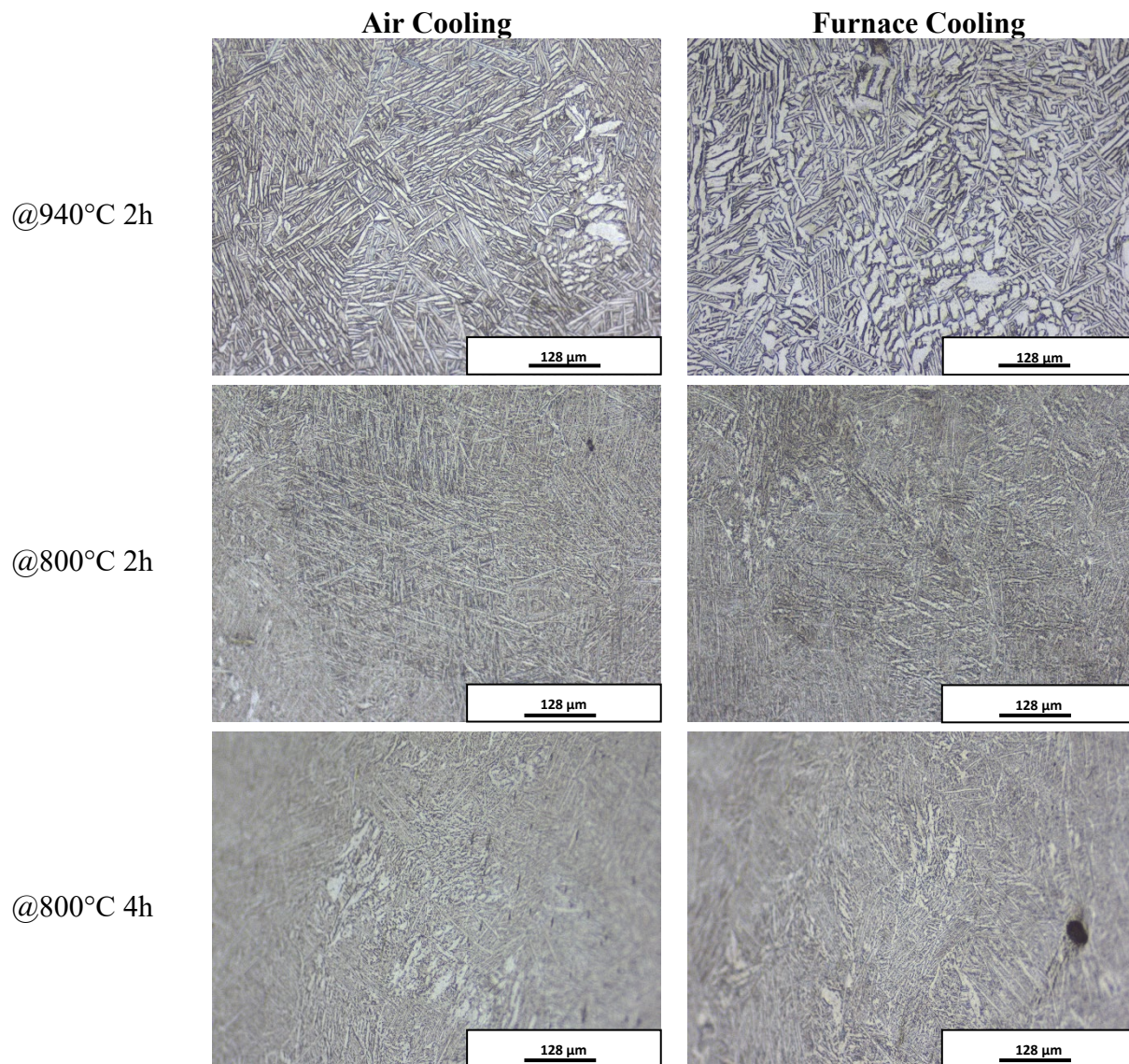


Figure 6: Effect of the cooling rate for L-PBF parts

The results reveal that cooling rate has no remarkable influence on microstructure except for the samples annealed at 940°C. Furnace cooling led to increased  $\alpha$  lath thickness and formation of globular  $\alpha$  colonies locally in the microstructure of the samples annealed at 940°C due to slow cooling rate than air cooling.

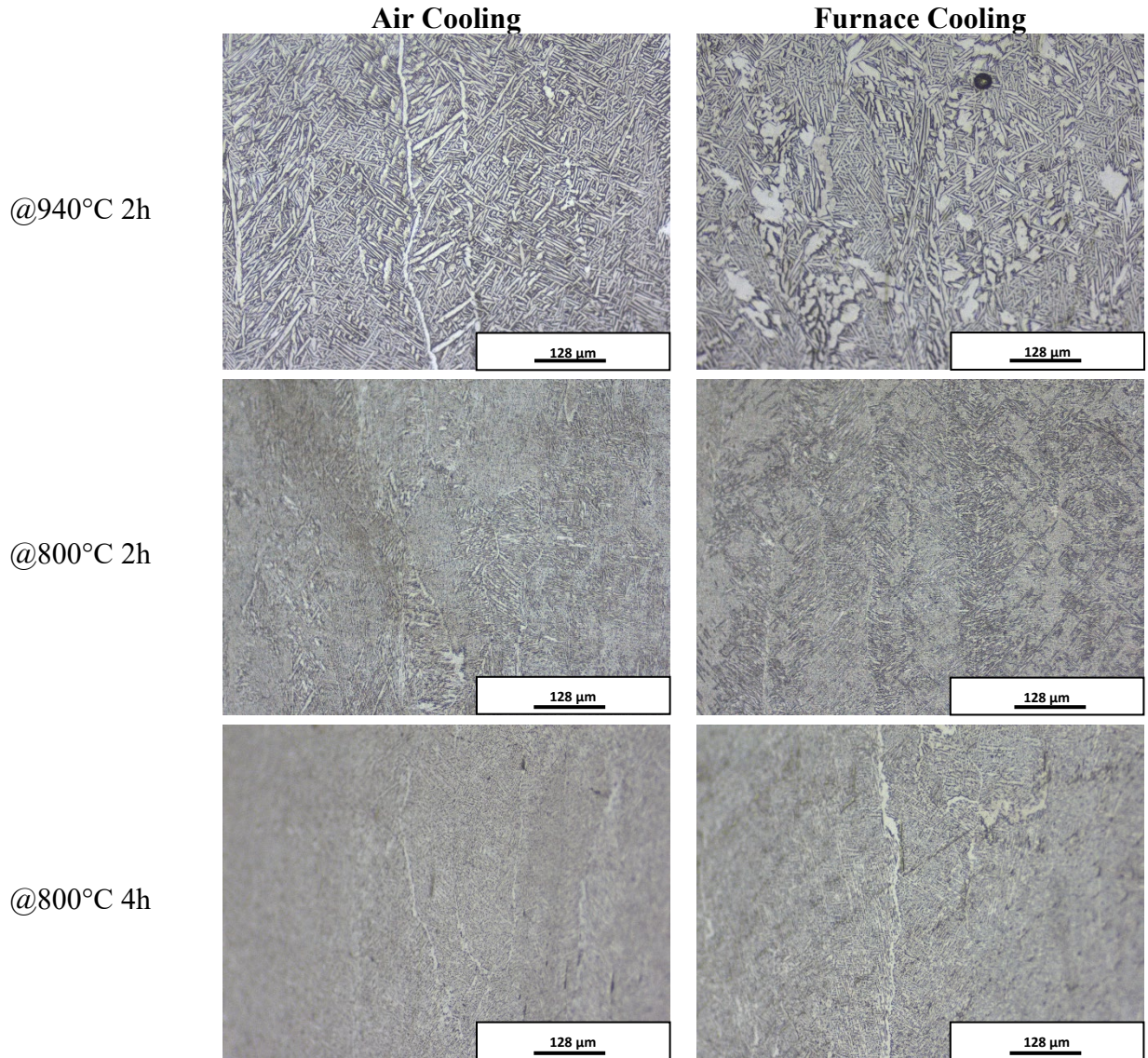


Figure 7: Effect of the cooling rate for E-PBF parts

### ***Oxidation and Hardness Results***

Titanium and its alloys are easily oxidized when exposed to elevated temperature and oxygen bearing conditions. Since the heat treatments were carried out in the open-air atmosphere in this study, the oxide layer formations were examined by OM images obtained from the edge of the heat treated samples. The overall oxide reaction consists of oxide formation and inward oxygen diffusion into the bulk material. This diffusion leads to an oxygen enriched layer, which is continuous, hard and brittle named as alpha-case layer, beneath the oxide scale. In this study, as expected, all heat treated samples are covered by an oxide layer. It is shown in the Figure 8 and 9 that increasing temperature and increasing duration led to a thicker oxide layer on the surface of the samples.

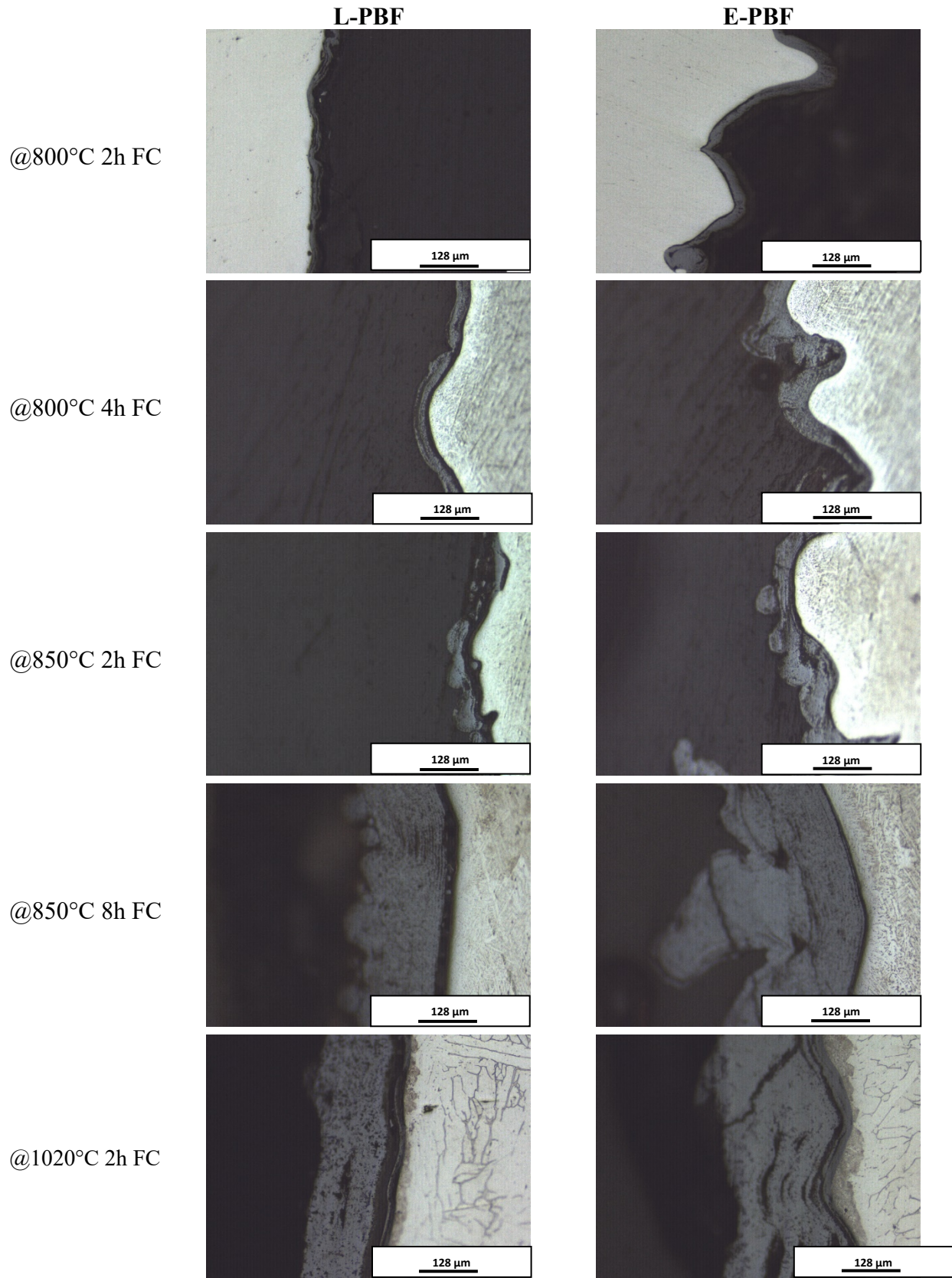


Figure 8: Oxide layer images of the heat treated samples

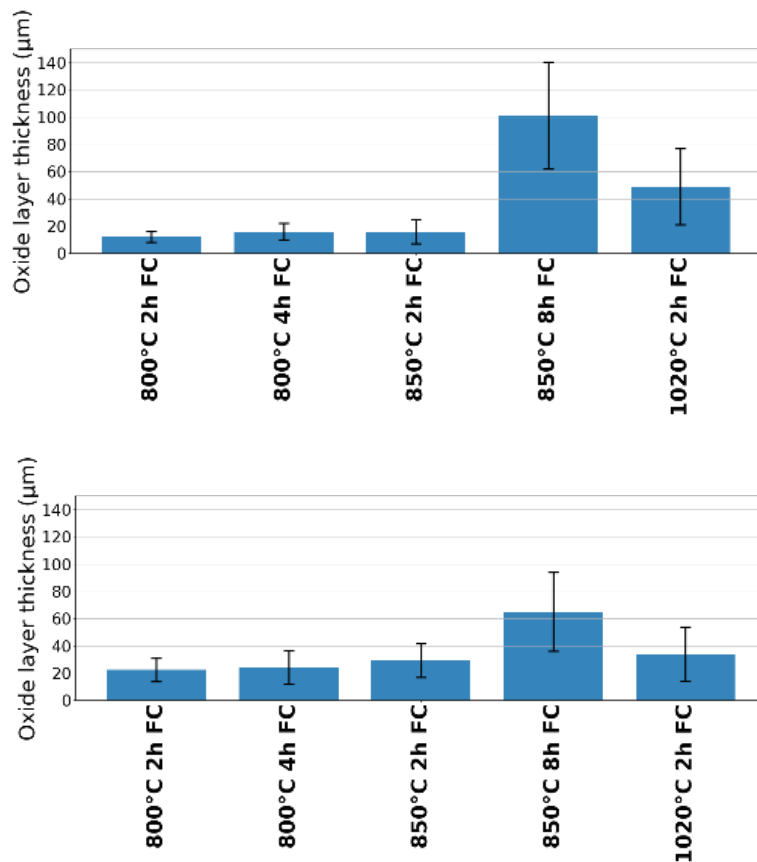


Figure 9: Oxide layer thicknesses of heat treated samples a) L-PBF b) E-PBF

In Figure 10, hardness results show that supertransus temperature annealed samples displayed extremely high hardness values (up to 500 HV) despite of high grain sizes in contrast to average hardness around 380 HV. Samples with larger grain sizes are normally expected to exhibit lower hardness values due to the Hall-Petch grain size effect [30]. Calculated grain sizes of the heat treated samples by image analysis are exhibited in Figure 11 and it can be seen from the Figure 11 that supertransus temperature heat treated samples have the highest grain sizes. It is important to note that the scatter of the grain size measurements increases as the grain size is increased especially at elevated temperatures. This is attributed to the measurement method and needs further investigations. Extremely high hardness values at elevated temperatures are thus not due to the grain size effect and attributed to oxygen diffusion inside the samples and hardening of the samples. In order to reveal the exact effects of heat treatment conditions on hardness, heat treatments will be conducted under a protective atmosphere as the future work.

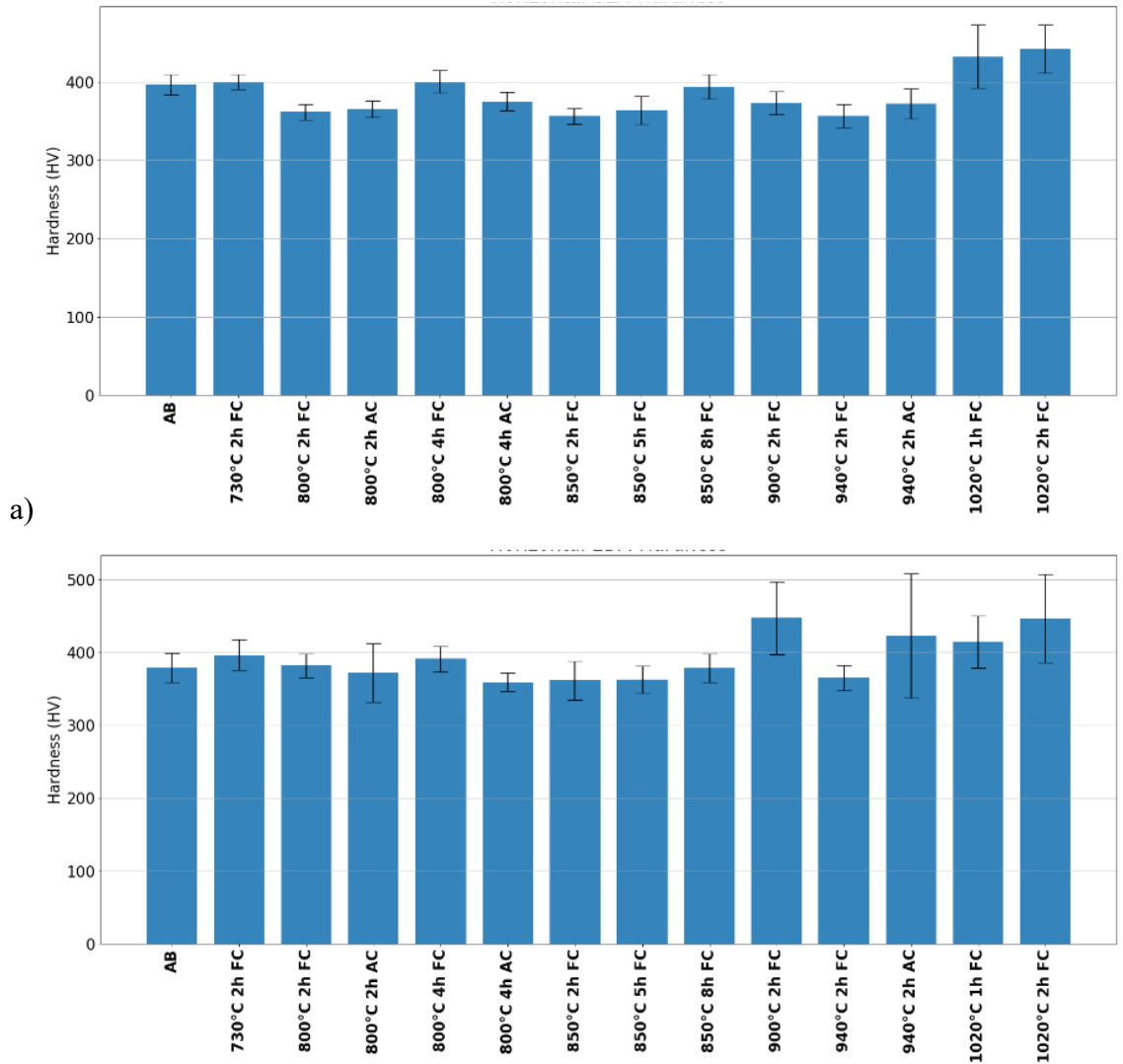


Figure 10: Hardness of the heat treated samples a) L-PBF b) E-PBF

### Conclusions

In this study, various heat treatment cycles were applied to L-PBF and E-PBF samples in order to reveal the effect the annealing temperature, duration and cooling rate in a wide range.

The main highlights of the study can be summarized as:

- From as-built microstructures, it is observed that while L-PBF sample exhibits a martensitic microstructure  $\alpha'$  acicular grains, E-PBF sample reveals lamellar  $\alpha+\beta$  basketweave (Widmanstätten) structure.
- The annealing temperature was varied between 730 and 1200 °C in this study. While lower temperatures (<900°C) have minor effect on microstructures and almost no visible difference from the as-built samples was observed while moderate annealing temperatures (900°C and 940°C) below the beta transus temperature modified microstructures to some extent. High temperature annealing transformed parent  $\beta$  columns to uniform equiaxed grains and needle-like  $\alpha$  laths to globular  $\alpha$  grains.

- Increasing annealing duration increases size of  $\alpha$  grains. The effect of duration is more pronounced at elevated temperatures.
- The results also reveal that cooling rate has only remarkable influence on microstructure for elevated temperatures.
- Heat treatments under ambient atmosphere led to a thin oxide scale layer and alpha-case layer. The diffusion of oxygen inwards the part greatly increased the microhardness values.

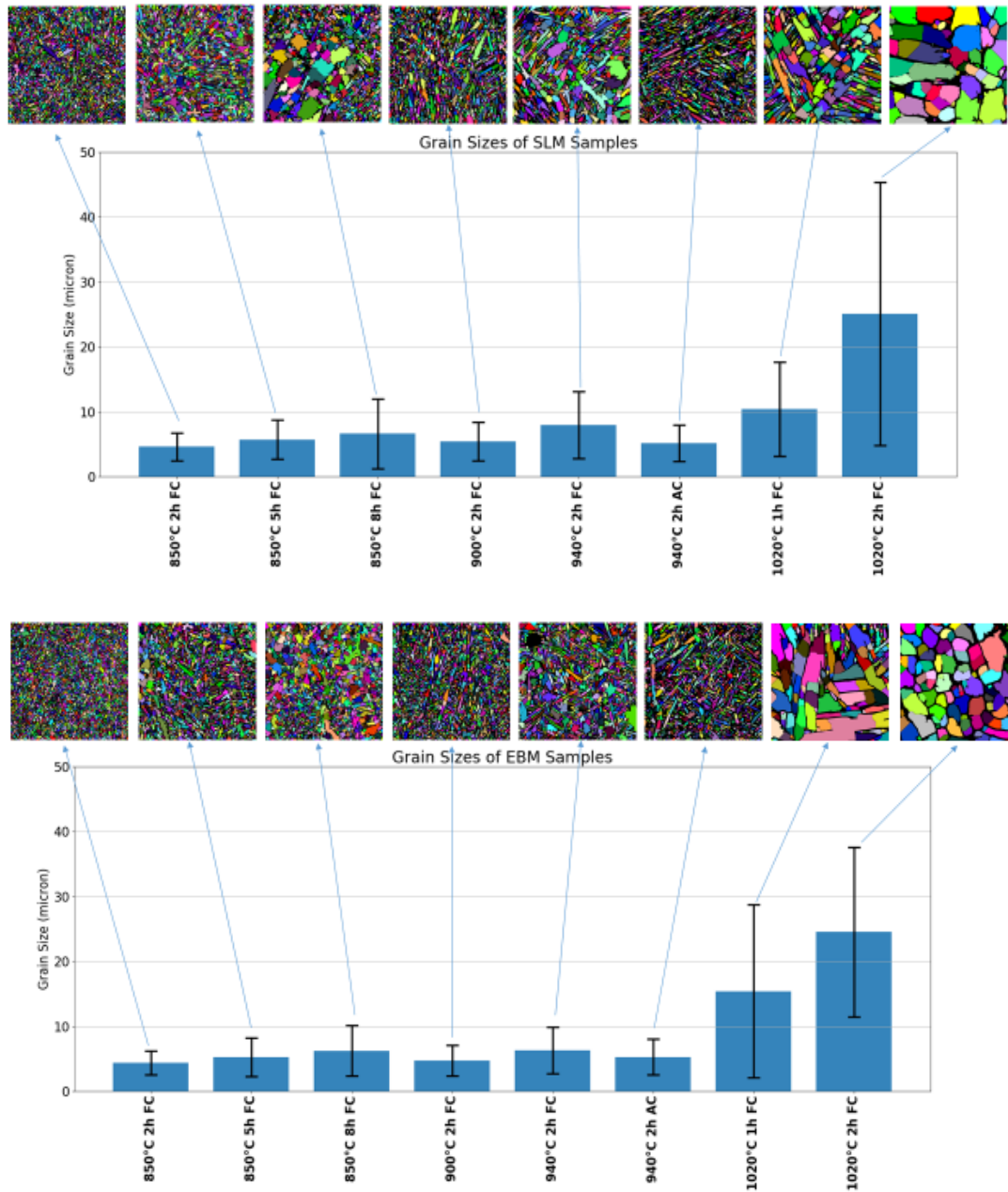


Figure 11: Grain size of the heat treated samples a) L-PBF b) E-PBF

## References

- [1] I. Astm, ASTM F2792-10: standard terminology for additive manufacturing technologies, ASTM International (2010).
- [2] A. Agapovichev, A. Sotov, V. Kokareva, V. Smelov, Possibilities and limitations of titanium alloy additive manufacturing, MATEC Web of Conferences, EDP Sciences, 2018, p. 01064.
- [3] Additive Manufacturing Machines, 2021. <https://www.ge.com/additive/additive-manufacturing/machines>. (Accessed June 18,2021).
- [4] M.G. Martinez, Metal Additive Manufacturing & Case Studies, 2016. <https://www.slideshare.net/Prizztech/metal-additive-manufacturing-manufacturing>. (Accessed June 6, 2021).
- [5] C.E. Olivier Rigo, Selective Laser Melting versus Electron Beam Melting, 2013. <https://www.slideshare.net/carstenengel/selective-laser-melting-versus-electron-beam-melting>. (Accessed June 18, 2021).
- [6] S. Liu, Y.C. Shin, Additive manufacturing of Ti6Al4V alloy: A review, Materials & Design 164 (2019) 107552.
- [7] R. Gupta, V.A. Kumar, C. Mathew, G.S. Rao, Strain hardening of titanium alloy Ti6Al4V sheets with prior heat treatment and cold working, Materials Science and Engineering: A 662 (2016) 537-550.
- [8] C. de Formanoir, A. Brulard, S. Vivès, G. Martin, F. Prima, S. Michotte, E. Rivière, A. Dolimont, S. Godet, A strategy to improve the work-hardening behavior of Ti–6Al–4V parts produced by additive manufacturing, Materials Research Letters 5(3) (2017) 201-208.
- [9] A.R. Prasad, K. Ramji, G. Datta, An experimental study of wire EDM on Ti-6Al-4V alloy, Procedia materials science 5 (2014) 2567-2576.
- [10] L. Parry, I. Ashcroft, R.D. Wildman, Understanding the effect of laser scan strategy on residual stress in selective laser melting through thermo-mechanical simulation, Additive Manufacturing 12 (2016) 1-15.
- [11] Ó. Teixeira, F.J. Silva, L.P. Ferreira, E. Atzeni, A Review of Heat Treatments on Improving the Quality and Residual Stresses of the Ti–6Al–4V Parts Produced by Additive Manufacturing, Metals 10(8) (2020) 1006.
- [12] G. Lütjering, J.C. Williams, Titanium, Springer Science & Business Media2007.
- [13] R. Huang, M. Riddle, D. Graziano, J. Warren, S. Das, S. Nimbalkar, J. Cresko, E. Masanet, Energy and emissions saving potential of additive manufacturing: the case of lightweight aircraft components, Journal of Cleaner Production 135 (2016) 1559-1570.
- [14] B. Wysocki, P. Maj, R. Sitek, J. Buhagiar, K.J. Kurzydłowski, W. Świążkowski, Laser and electron beam additive manufacturing methods of fabricating titanium bone implants, Applied Sciences 7(7) (2017) 657.
- [15] Y. Zhai, H. Galarraga, D.A. Lados, Microstructure, static properties, and fatigue crack growth mechanisms in Ti-6Al-4V fabricated by additive manufacturing: LENS and EBM, Engineering failure analysis 69 (2016) 3-14.
- [16] H. Galarraga, D.A. Lados, R.R. Dehoff, M.M. Kirka, P. Nandwana, Effects of the microstructure and porosity on properties of Ti-6Al-4V ELI alloy fabricated by electron beam melting (EBM), Additive Manufacturing 10 (2016) 47-57.

- [17] M. Koike, P. Greer, K. Owen, G. Lilly, L.E. Murr, S.M. Gaytan, E. Martinez, T. Okabe, Evaluation of titanium alloys fabricated using rapid prototyping technologies—electron beam melting and laser beam melting, *Materials* 4(10) (2011) 1776-1792.
- [18] M. Simonelli, Y.Y. Tse, C. Tuck, The formation of  $\alpha + \beta$  microstructure in as-fabricated selective laser melting of Ti-6Al-4V, *Journal of Materials Research* 29(17) (2014) 2028-2035.
- [19] B.J. Hayes, B.W. Martin, B. Welk, S.J. Kuhr, T.K. Ales, D.A. Brice, I. Ghamarian, A.H. Baker, C.V. Haden, D.G. Harlow, Predicting tensile properties of Ti-6Al-4V produced via directed energy deposition, *Acta Materialia* 133 (2017) 120-133.
- [20] T. Vilaro, C. Colin, J.-D. Bartout, As-fabricated and heat-treated microstructures of the Ti-6Al-4V alloy processed by selective laser melting, *Metallurgical and materials transactions A* 42(10) (2011) 3190-3199.
- [21] G. Kasperovich, J. Hausmann, Improvement of fatigue resistance and ductility of TiAl6V4 processed by selective laser melting, *Journal of Materials Processing Technology* 220 (2015) 202-214.
- [22] V. Chastand, P. Quaegebeur, W. Maia, E. Charkaluk, Comparative study of fatigue properties of Ti-6Al-4V specimens built by electron beam melting (EBM) and selective laser melting (SLM), *Materials Characterization* 143 (2018) 76-81.
- [23] J. Pegues, S. Shao, N. Shamsaei, N. Sanaei, A. Fatemi, D. Warner, P. Li, N. Phan, Fatigue of additive manufactured Ti-6Al-4V, Part I: The effects of powder feedstock, manufacturing, and post-process conditions on the resulting microstructure and defects, *International Journal of Fatigue* 132 (2020) 105358.
- [24] M.-W. Wu, J.-K. Chen, B.-H. Lin, P.-H. Chiang, M.-K. Tsai, Compressive fatigue properties of additive-manufactured Ti-6Al-4V cellular material with different porosities, *Materials Science and Engineering: A* 790 (2020) 139695.
- [25] A. Sharma, M.C. Oh, J.-T. Kim, A.K. Srivastava, B. Ahn, Investigation of electrochemical corrosion behavior of additive manufactured Ti-6Al-4V alloy for medical implants in different electrolytes, *Journal of Alloys and Compounds* 830 (2020) 154620.
- [26] M. Wang, Y. Wu, S. Lu, T. Chen, Y. Zhao, H. Chen, Z. Tang, Fabrication and characterization of selective laser melting printed Ti-6Al-4V alloys subjected to heat treatment for customized implants design, *Progress in Natural Science: Materials International* 26(6) (2016) 671-677.
- [27] Y.-K. Kim, S.-H. Park, J.-H. Yu, B. AlMangour, K.-A. Lee, Improvement in the high-temperature creep properties via heat treatment of Ti-6Al-4V alloy manufactured by selective laser melting, *Materials Science and Engineering: A* 715 (2018) 33-40.
- [28] M. Kusano, S. Miyazaki, M. Watanabe, S. Kishimoto, D.S. Bulgarevich, Y. Ono, A. Yumoto, Tensile properties prediction by multiple linear regression analysis for selective laser melted and post heat-treated Ti-6Al-4V with microstructural quantification, *Materials Science and Engineering: A* 787 (2020) 139549.
- [29] L. Facchini, E. Magalini, P. Robotti, A. Molinari, S. Höges, K. Wissenbach, Ductility of a Ti-6Al-4V alloy produced by selective laser melting of prealloyed powders, *Rapid Prototyping Journal* (2010).
- [30] E. Hall, The deformation and ageing of mild steel: III discussion of results, *Proceedings of the Physical Society. Section B* 64(9) (1951) 747.